Direct detection and characterization of vortices in optical speckle

Master's thesis

Yorick O. van Boheemen

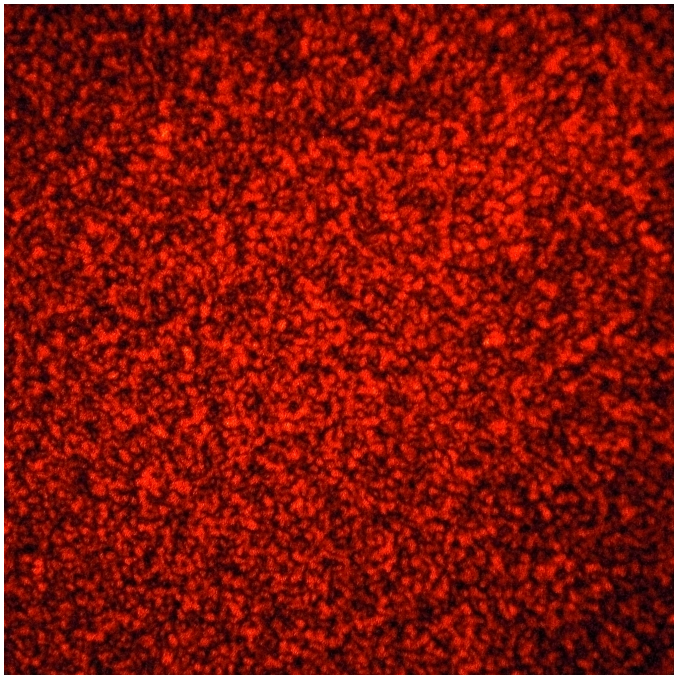

August 30, 2011

Leiden University
Huygens Laboratory
Group: Quantum Optics

Supervisors:
Martin P. van Exter
Gregorius C.G. Berkhout

Contents

Chapter 1

Introduction

1.1 Optical speckle

Speckle is a common phenomenon in optics. It can be synthesized by a random coherent superposition of many plane waves which results in a 'speckled' pattern of light and dark spots. A common way of producing speckle is by illuminating a rough surface with a laser beam.

So called optical vortices constitute special points in the speckle pattern, where the amplitude of the field is zero and the phase is singular. Since the field is continuous, vortices are embedded in the darker regions of the speckle pattern. Around a vortex the phase varies from 0 to $2\pi m$, where m is called the vortex charge. Although in principle m could take on any integer value, in speckle patterns one usually finds $m = \pm 1$. Higher order vortices can occur but are extremely rare [1].

For an isotropic vortex the phase varies linearly on a circular contour centered around the vortex. For this type of vortex the complex field amplitude in the plane perpendicular to the propagation direction of the light can be described locally with $E \sim re^{i\phi}$, where r is the distance from the vortex and ϕ the polar angle. However, a vortex in a speckle pattern is in general not isotropic. Several attempts have been made to characterize anisotropic vortices [2]-[4]. This anisotropy is characterized by an elliptic contour over which the phase varies linearly and the intensity is constant. Following [3], we will argue that the vortex can best be described in terms of the ellipticity and orientation of this contour. We will also introduce an alternative description in terms of the Poincaré sphere.

1.2 Probing a speckle field

At optical frequencies it is impossible to directly measure the phase of light. Hence, the detection of vortices traditionally relied on interferometric techniques [5, 6]. We will use a Multi-Point Interferometer (MPI) [7] as a tools

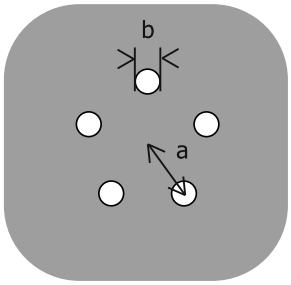

Figure 1.1: The Multi-Pinhole Interferometer (MPI) consists of a circle of radius a, with N evenly spaced circular holes in it. The holes have diameter b. In our experiment, $N = 5$, $a = 100$ µm and $b = 50$ µm.

to directly detect the phase profile of the light. More traditional methods for the detection of a phase profile rely heavily on interferometric techniques. Using an MPI has the advantage that it does not require any additional interferometric set-up.

An MPI (see figure 1.1) consists of a number of small pinholes distributed uniformly in a circular configuration. Light that falls through the pinholes will diffract to form an interference pattern. This interference pattern can be used to extract the relative phases of the light on the individual pinholes [8] and determine the local vorticity in the incident light [7]. We will expand on the existing analysis [8] by fully solving the complex amplitudes on the detection circle, apart from an arbitrary phase.

Since the MPI is smaller than the average speckle size, the field can be expanded in terms of its derivatives. These derivatives can be used to characterize the optical vortices present in the speckle pattern. Measurement at multiple positions allows for the resolving of an entire speckle field.

1.3 Overview of thesis

This thesis attempts to develop a theory for the description of vortices and the statistics of a speckle field and to measure a speckle field with an MPI to test the theory.

Chapter 2 aims to explain general properties of the speckle field in general and of the vortices in particular. This theory uses the fact that the measurement of the speckle field is local, such that the description can be done in terms of the local optical field and its first-order spatial derivatives. The expressions derived in this chapter which will be used in simulations and experiments. We will not discuss how this should be measured until chapter 4.

In chapter 3 we present simulations of an optical speckle field, both to increase our understanding of speckle patterns and to apply the theory of

the previous chapter in a situation where we have complete information: a phase-resolved speckle field. This chapter therefore constitutes both a validation of the theory of the previous chapter and, more importantly, a prediction for the experiment.

In chapter 4 we will discuss how to obtain the local speckle field experimentally. The interference patterns generated by the MPI can be used to obtain the electric fields at the location of the pinholes of the MPI, up to an arbitrary phase. This allows us to observe the properties of individual vortices and of the statistics of the speckle pattern.

Chapter 5 discusses an explanation of the experimental set-up. This set-up comprises an MPI, that can be tranlsated in the plane orthogonal to the propagation direction of the speckle field, to allow a scan of a 2D-section of the speckle field.

To support the validity of our method, chapter 6 presents the experimental results of measurements on an isotropic vortex beam. Such a beam is produced by a fork hologram. Fork holograms, when illuminated with a laser beam, produce a far-field diffraction pattern with an optical vortex in each of the diffraction orders. We observe that the experiment on a vortex beam yields the desired results. This supports the theory laid out in the first chapters.

In chapter 7 we present the results of similar experiments, performed on optical speckle patterns. We will treat the properties of the vortices in the speckle pattern in a statistical fashion, leaning heavily on the theory of chapter 2 and compare the results to the simulations from chapter 3.

In the last chapter, chapter 8, we will summarize our findings and give a brief outlook for possible future experiments.

Chapter 2

General theory

This chapter aims to explain the properties of the speckle field in general and of the vortices in particular. In this chapter expressions are derived which will be used in simulations and experiments.

2.1 Expansion of the electric field

We will probe the field pattern on a scale that is much smaller than the average speckle size. Therefore, we are allowed to expand the complex electric field up to first order.

$$E(x,y) = E(x_0,y_0) + \Delta x \left.\frac{\partial E}{\partial x}\right|_{x_0,y_0} + \Delta y \left.\frac{\partial E}{\partial y}\right|_{x_0,y_0}. \tag{2.1}$$

We can define the alternative circular derivative

$$\alpha_{\pm} = \frac{1}{2}\left(\frac{\partial E}{\partial x} \mp i\frac{\partial E}{\partial y}\right). \tag{2.2}$$

Now the first order terms can be written as

$$E(r,\phi) = \alpha_0 + \Delta r(\alpha_+ e^{+i\phi} + \alpha_- e^{-i\phi}), \tag{2.3}$$

where $\alpha_0 = E(x_0,y_0)$ [9]. Thus α_+ and α_- are the derivative with respect to the $l=+1$ and $l=-1$ component of the vortices. For an optical vortex the ratio

$$z = \frac{\alpha_-}{\alpha_+} \tag{2.4}$$

determines the sign of the vortex charge. When $|z|<1$, the phase rotates counterclockwise, which we identify with a vortex charge of $m=+1$. When $|z|>1$, the phase rotates clockwise and $m=-1$.

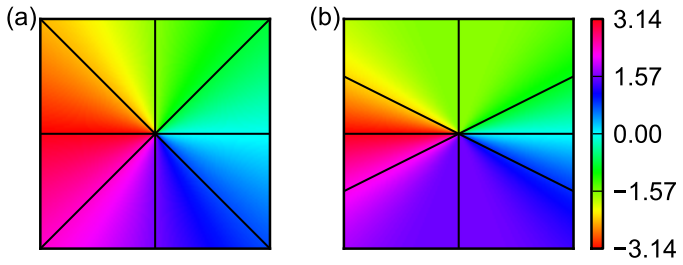

Figure 2.1: Lines of equal phase of (a) an isotropic and (b) anisotropic $l = -1$ vortex. Consecutive phase lines differ by a phase of $\pi/4$. The colour indicates the phase of the field.

2.2 Properties of an optical vortex

An isotropic vortex can be described with $E \sim re^{\pm i\phi}$. The phase gradient is linear from 0 to 2π on a circle around the vortex. This is depicted in figure 2.1(a). For a general vortex in a speckle pattern the field is a linear combination of $e^{+i\phi}$ and $e^{-i\phi}$ as in equation (2.3). The weights of the $m = +1$ and $m = -1$ vortex are given by the moduli of α_+ and α_-, respectively.

We can construct contours of constant intensity around the vortex in the following way. First, rewrite the field to

$$E(x, y) = (\alpha_+ + \alpha_-)x + i(\alpha_+ - \alpha_-)y, \tag{2.5}$$

where we take $\alpha_0 = 0$ for convenience. To obtain coordinate axes which coincide with the axes of the ellipse, we split off the phase of the prefactors

$$\begin{aligned} x' &= x\, e^{i \arg(\alpha_+ + \alpha_-)} \\ y' &= y\, e^{i \arg(\alpha_+ - \alpha_-)}. \end{aligned} \tag{2.6}$$

We can now write

$$I_c = |\alpha_+ + \alpha_-|^2 x'^2 + |\alpha_+ - \alpha_-|^2 y'^2. \tag{2.7}$$

This contour takes the form of an ellipse and reduces to a circle for a pure vortex (i.e. either $\alpha_+ = 0$ or $\alpha_- = 0$). The phase ϕ increases linearly on this ellipse. The phase profile of an elliptic vortex is depicted is figure 2.1(b).

The parameters that characterize an optical vortex are therefore the eccentricity ϵ and the orientation ϕ_0 (see figure 2.2).

Other characterizations of vortices have been proposed. For instance, Freund et al. [2] introduced the terms anisotropy and skewness. However, these properties are not mutually independent and can be altered by adding an overall phase factor to the complex field. Schechner et al. [3] pointed this

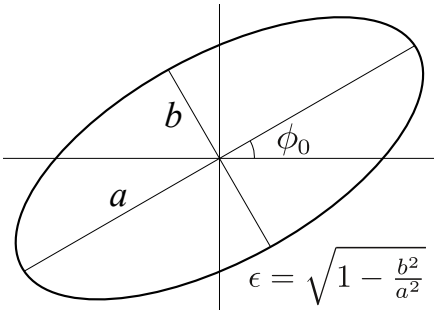

Figure 2.2: Properties of an ellipse. We will describe these with two parameters, the ellipticity ϵ and the orientation ϕ_0.

out and introduced the anisotropy of the vortex and the orientation of the semi-major axis of the ellipse as the truly independent parameters. These properties have been further described in [6, 9].

The probability distributions of these properties in a speckle field have also been discussed in [9]. Since the speckle pattern is isotropic, the probability distribution of ϕ_0 is expected to be uniform on the interval $[0, \pi]$. The probability distribution of ϵ is [9]

$$P(\epsilon^2) = \frac{4\epsilon^2}{(2-\epsilon^2)^3}, \tag{2.8}$$

$$P(\epsilon) = \frac{d\epsilon^2}{d\epsilon} P(\epsilon^2) = \frac{8\epsilon^3}{(2-\epsilon^2)^3}. \tag{2.9}$$

Now we want to express these parameters in terms of the circular derivatives $\alpha_\pm$. This was also done in [9]:

$$\begin{aligned} \epsilon^2 &= \frac{4|\alpha_+||\alpha_-|}{(|\alpha_+| + |\alpha_-|)^2} \\ \phi_0 &= \tfrac{1}{2}(\arg\alpha_+ - \arg\alpha_-) \end{aligned} \quad . \tag{2.10}$$

From these equations it is easily seen that α_+ and α_- fully describe the ellipse, since these are the only parameters determining ϵ and ϕ_0.

2.3 The Poincaré sphere

The Poincaré sphere is well known for its description of polarization. It can however also be used to describe vortex states [9]. The Poincaré sphere is depicted in figure 2.3. The north and south pole correspond to isotropic vortices, while the rest of the sphere corresponds to anisotropic vortices of various orientations.

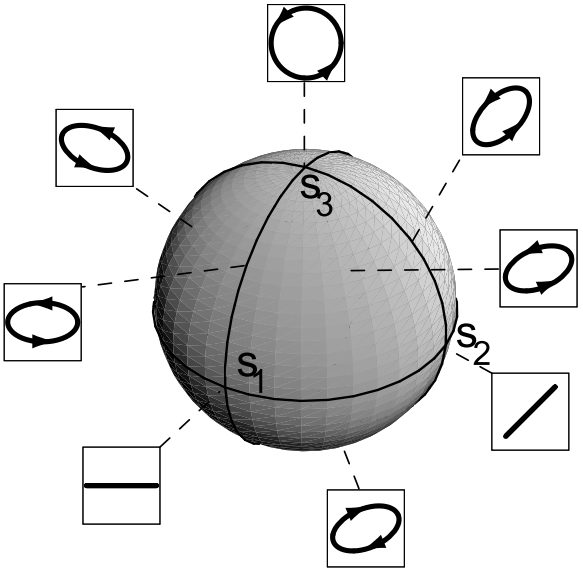

Figure 2.3: The Poincaré sphere. The north pole corresponds to a circular vortex of charge $m = +1$, while the south pole corresponds to a circular $m = -1$. The equator depicts linear vortices, more reminiscent of Hermite-Gauss type modes. Image taken from [9].

The normalized Stokes vectors can be expressed either in terms of the parameters ϵ and ϕ_0 [9], or in terms of the circular derivatives α_+ and α_- as

$$\begin{aligned} s_3 = \pm\frac{2\sqrt{1-\epsilon^2}}{2-\epsilon^2} &= \frac{|\alpha_+|^2 - |\alpha_-|^2}{|\alpha_+|^2 + |\alpha_-|^2} \\ \frac{s_2}{s_1} = 2\tan\phi_0 &= 2\tan\tfrac{1}{2}(\arg\alpha_+\alpha_-^*) \end{aligned} \quad . \tag{2.11}$$

For isotropic speckle patterns it has been shown in [9] that equal areas on the Poincaré shpere have equal probability [9]. This also means that it is uniform in any direction, for instance in the direction s_3. The probability distribution of s_3 over the interval $[-1, 1]$ is thus

$$P(s_3) = \tfrac{1}{2}. \tag{2.12}$$

When we only look at vortices, different statistics apply. We can now for instance look at the probability distribution for s_3^2. We can relate this to the expression for $P(\epsilon^2)$ in equation (2.9) by

$$P(s_3^2) = P(\epsilon^2)\left|\frac{d\epsilon^2}{ds_3^2}\right|. \tag{2.13}$$

When we use the expression for s_3 in equation 2.11 we obtain

$$P(s_3^2) = 1. \tag{2.14}$$

This means the vortex properties are uniformly distributed in s_3^2, over the interval $[0, 1]$.

In this chapter we derived expressions for what we argued to be the fundamental properties of vortices in terms of derivatives of the field α_+ and α_-. In chapter 4 we will discuss how to obtain these derivatives experimentally.

Chapter 3

Simulations

In this chapter we present simulations of an optical speckle field, both to increase our understanding of speckle patterns and to apply the theory presented in the previous chapter in a situation where we have complete information: a phase-resolved speckle field. This chapter therefore constitutes both a validation of theory and, more importantly, a prediction for the experiment.

The speckle field was simulated as follows. First we created a grid with random complex numbers, distributed uniformly on a disc of radius unity in the complex plane. This grid is then convoluted by means of Fourier transformation with a Gaussian amplitude function to create a smooth speckle field. The width of the Gaussian in k-space is used to control the average speckle size after Fourier transformation and the number of vortices in real-space.

The derivatives $\partial_x E$ and $\partial_y E$ of the field are determined by the difference between adjacent pixels in the x- and y-direction, respectively. These derivatives are then rewritten to $\alpha_\pm$, as in equation (2.2).

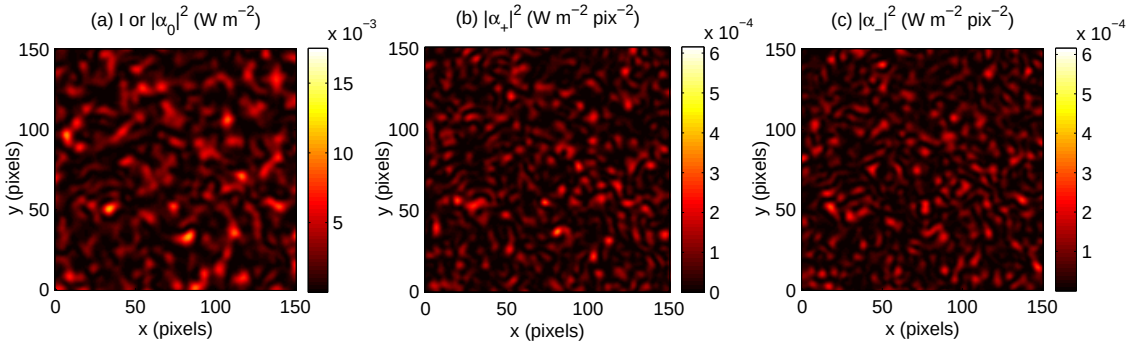

Figure 3.1: A speckle field was simulated of 1000 × 1000 pixels. Depicted are 150×150 pixels cut-outs of (a) the intensity of the field and (b)-(c) the circular derivatives $|\alpha_+|^2$ and $|\alpha_-|^2$.

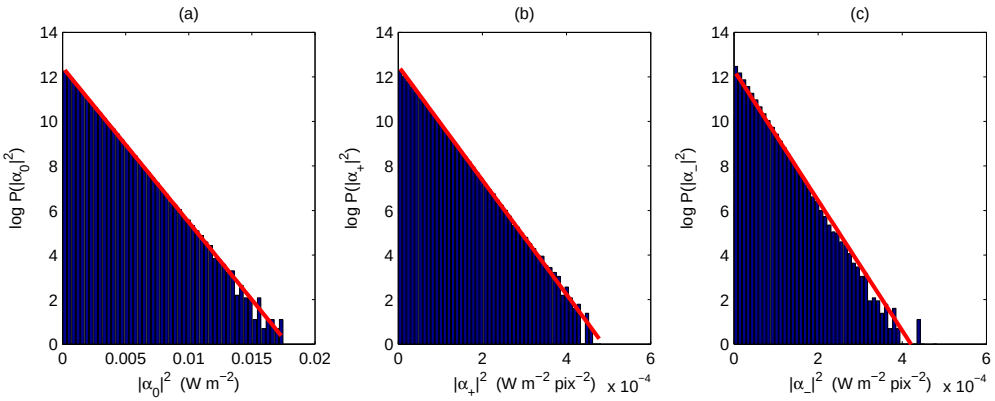

Figure 3.2: Distributions of the simulated speckle field from figure 3.1. As expected, the intensity $I = |\alpha_0|^2$, depicted in (a), obeys an exponential probability distribution. The red line is a fit, yielding an average value $W_0 = \langle I \rangle = 1.44 \times 10^{-3}$ W m^{-2}. In (b) $|\alpha_+|^2$ and (c) $|\alpha_-|^2$ show the same behaviour, with average values of $W_{\alpha_+} = 3.90 \times 10^{-5}$ W m^{-2} pixel^{-2} and $W_{\alpha_-} = 3.42 \times 10^{-5}$ W m^{-2} pixel^{-2}.

3.1 Field derivatives

In figure 3.1(a) the intensity of the simulated speckle pattern is plotted, alongside the 'intensity' of the derivatives, in 3.1(b) and (c). At first glance, $|\alpha_+|^2$ and $|\alpha_-|^2$ look like a speckle pattern as well, albeit with a smaller speckle size. We will use statistic tools to investigate this claim.

It is well known [10] that the intensity of a speckle pattern shows exponential statistical behaviour. In figure 3.2(a) this result is reproduced. The probability distribution is given by

$$P(I) = P_0 e^{-I/W_0} \tag{3.1}$$

where P_0 is a normalization constant and $W_0 = \langle I \rangle$ is the average value of the intensity. Figures 3.2 (b) and (c) show interestingly enough the same statistical behaviour for $|\alpha_+|^2$ and $|\alpha_-|^2$. So expressions similar to 3.1 can be written down for $|\alpha_+|^2$ and $|\alpha_-|^2$. The values $\langle |\alpha_{pm}|^2 \rangle$ are obtained by a linear fit of log $P(I)$.

Here we introduce the width of the speckle W for the different modes. In principle the $\alpha_\pm$ are derivatives, so these have units equal to those of α_0 divided by distance [pixel]. We consider the ratio of widths, which is

$$\begin{aligned} W_0/W_{\alpha_+} &= 36.9 \text{ pixel}^2 \\ W_0/W_{\alpha_-} &= 42.0 \text{ pixel}^2 \end{aligned}$$

It would be expected from their definitions in chapter 2 that α_+ and α_+ are statistically independent. To verify this we use a concept from quantum

mechanics, called the fidelity of states. It is a measure of the "closeness" of two quantum states:

$$F\big(|\psi\rangle, |\phi\rangle\big) = \langle\psi|\phi\rangle \tag{3.2}$$

where we assume both states to be normalized. The fidelity gives 1 if the two states are equal and 0 if the states are orthogonal. We can generalize this in terms of the normalized probability distributions $P\big(|\alpha_+|^2, |\alpha_-|^2\big)$ and $P\big(|\alpha_+|^2\big)\cdot P\big(|\alpha_-|^2\big)$. These distribution functions are equal if $|\alpha_+|^2$ and $|\alpha_-|^2$ are statistically independent, in which case the fidelity should give 1. We calculate the integral

$$F = \int \sqrt{P\big(|\alpha_+|^2, |\alpha_-|^2\big)}\ \sqrt{P\big(|\alpha_+|^2\big)P\big(|\alpha_-|^2\big)}\ d|\alpha_+|^2 d|\alpha_-|^2. \tag{3.3}$$

For the speckle field of figure 3.1 this calculation yields a fidelity of $F = 0.99986$. Thus, according to simulations α_+ and α_- are indeed statistically independent, as expected.

Now we return to the question whether the derivatives of the field α_+ and α_- form a speckle pattern similar to that of the field itself. We saw that these have the same probability distributions. However, this only gives information about the distribution of the complex amplitudes, but not about the shape of the spots. To this end, the auto-correlation functions $\langle E^*(\vec{x})E(\vec{x}+\Delta\vec{x})\rangle$ of the speckle pattern should be considered. Since we work in the plane orthogonal to the direction of propagation, the vectors are $\vec{x} = (x, y)$ and $\vec{k} = (k_x, k_y)$.

First, we note that we can expand a speckle field in its Fourier domain

$$E(\vec{x}) = \int f(\vec{k}) e^{i\vec{k}\cdot\vec{x}} d\vec{k}. \tag{3.4}$$

Then we can rewrite the auto-correlation function

$$\big\langle E^*(\vec{x})E(\vec{x}+\Delta\vec{x})\big\rangle = 2\pi \int |f(\vec{k})|^2 e^{i\vec{k}\cdot\vec{x}} d\vec{k}. \tag{3.5}$$

Since we used a Gaussian profile as input of the simulations, the Fourier components are simply $|f(\vec{k})|^2 \sim e^{-|\vec{k}|^2/\Delta k^2}$ where Δk^2 is the width of the Fourier component. The correlation function then becomes

$$\big\langle E^*(\vec{x})E(\vec{x}+\Delta\vec{x})\big\rangle \sim e^{-|\vec{x}|^2\Delta k^2/4}. \tag{3.6}$$

When we consider the correlation function for the derivatives of the field, we obtain

$$\big\langle \alpha_\pm^*(\vec{x})\alpha_\pm(\vec{x}+\Delta\vec{x})\big\rangle \sim \frac{\Delta k^2}{4}\left(1 - \frac{|\vec{x}|^2\Delta k^2}{4}\right) e^{-|\vec{x}|^2\Delta k^2/4}. \tag{3.7}$$

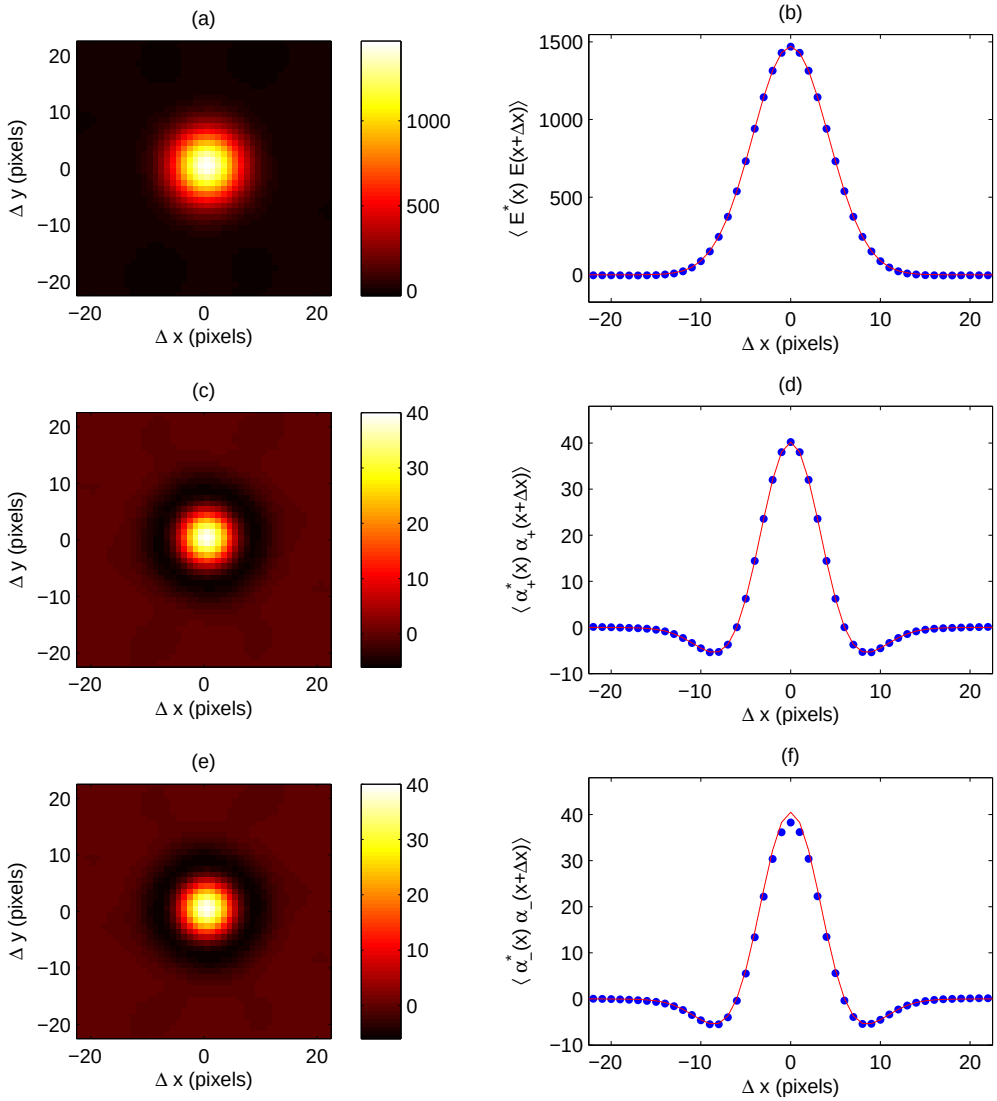

Figure 3.3: A 2×2 mm cut-out of the auto-correlation functions of (a) the speckle field E, (c) α_+ and (e) α_-. The graphs (b), (d) and (f) show cross-sections along the x-axis of the figures on the left. The dots show the simulation values, the lines depict the analytical curve fitted to the data. The fit parameters are mutually consistent. These figures are obtained from the speckle field of figure 3.1.

So we expect the correlation functions of the derivatives to display a different profile than the speckle field itself.

These correlation functions are calculated numerically from the simulated speckle pattern and plotted in figure 3.3. The figures on the left are false colour plots of the correlation functions over the two-dimensional speckle field. The graphs on the right are cut-outs along the x-axis, where the dots are the numerical values. We fitted equations (3.6) and (3.7) to the numerical values to obtain the value for Δk^2. The fits are depicted in figure 3.3(b), (d) and (f). They show excellent agreement with the simulated values. The obtained values for Δk^2 are

Correlation function	Δk
$\langle E^*(\vec{x})E(\vec{x}+\Delta\vec{x})\rangle$	0.33426 pixel^{-1}
$\langle \alpha_+^*(\vec{x})\alpha_+(\vec{x}+\Delta\vec{x})\rangle$	0.33259 pixel^{-1}
$\langle \alpha_-^*(\vec{x})\alpha_-(\vec{x}+\Delta\vec{x})\rangle$	0.33254 pixel^{-1}

These values are in good correspondence with one another. It is remarkable to see that the correlation function of the $\alpha_\pm$ shows a slight anticorrelation at around $\Delta x = 8$ pixels. This could correspond with observations of attracting and repelling vortices [12].

3.2 Vortex parameters

In the previous section we have discussed the speckle pattern and its derivatives in general. Now we turn our attention to the special points in the speckle pattern: the optical vortices. A vortex is defined by the presence of a phase discontinuity, around which the phase rotates. To determine if a point in the speckle field is a vortex, one has to look at the pixels surrounding that point. For isotropic vortices one could fit a line through a plot of phase versus angle, thus determining the vorticity [8]. For anisotropic vortices, this is not an accurate method, as the phase gradient is not linear with angle. This forms a non-linear curve, such that the slope of a fitted line would vary greatly with the choice for the zero of the angle.

Instead we use a condition also used in phase unwrapping of a signal. We will therefore call it the "phase unwrapping method." We consider eight pixels surrounding the pixel of interest. Their phases are defined in the interval $[-\pi, \pi]$. We calculate the phase difference between each pair of neighbouring pixels. When the phase difference between two neighbouring pixels is larger than π (or smaller than $-\pi$), we assign a value of -1 (or $+1$). The contributions from all the eight pixels are added to obtain the actual vortex charge at the central pixel. This way we exclude any discontinuities that are due to anisotropies or noise, which is relevant for the experiments.

In the previous chapter we saw that we could express the parameters of an optical vortex, namely ϵ and ϕ_0, in terms of $\alpha_\pm$ (Eq. (2.10)). We use

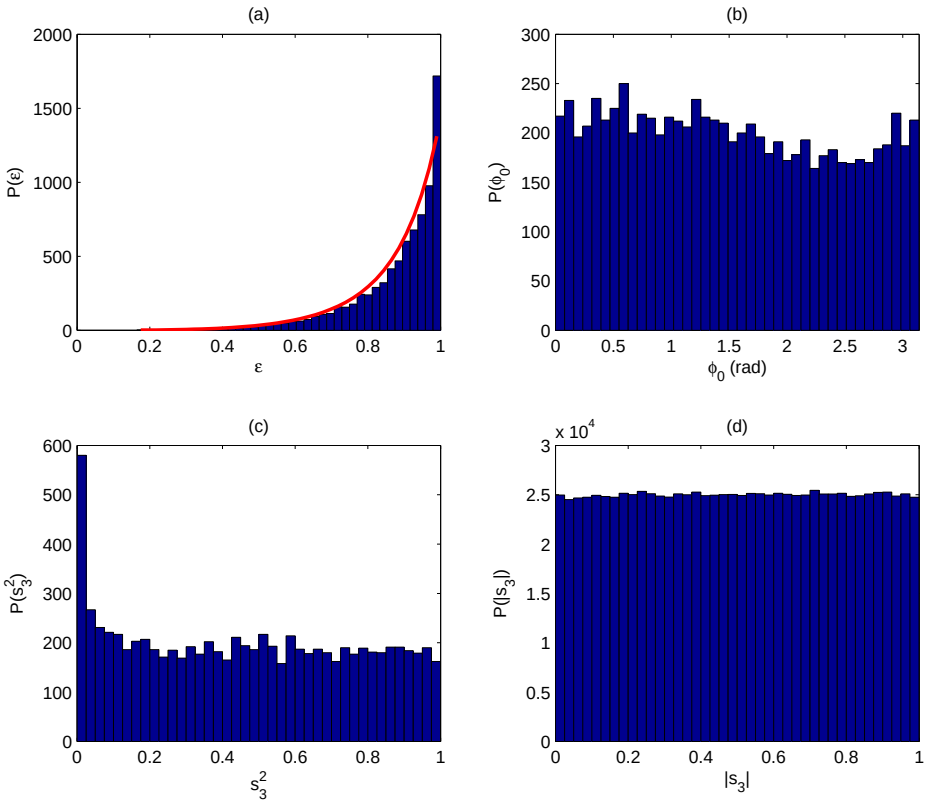

Figure 3.4: Four probability distributions of vortex properties in the simulated speckle field. The distributions of the two independent vortex parameters ϵ and ϕ_0 are depicted in (a) and (b), respectively. Figure (c) shows the (almost) uniform distribution of s_3^2 at the vortex locations. Figure (d) shows that $|s_3|$ is approximately uniform when averaged over the whole speckle field (note the increased occurrences on the vertical scale).

this relation to construct the probability distributions of these properties of vortices in the simulated speckle pattern. These are shown in figure 3.4(a) and (b). The theoretical distribution for ϵ given by equation 2.9 is plotted as a red line in figure 3.4(a). As mentioned in the previous chapter, the orientation ϕ_0 is expected to be uniform from 0 to π. This also holds for the simulations, since we introduce no anisotropies in the construction of the speckle pattern.

The description in terms of Stokes vectors lead to the prediction in equation (2.14), namely that $P(s_3^2)$ at the vortices is uniform. This is clearly visible in figure 3.4(c). There is, however, one clear, anomalous peak in the histogram. This would suggest a preference for vortices with $s_3^2 = 0$. These vortices lie on the equator of the Poincaré sphere. In terms of an ellipse, these vortices are highly eccentric (ϵ almost 1). It is as yet unclear why this seems to be the case.

Finally, we check the observation of the previous chapter that the whole speckle field is distributed uniformly over the Poincaré sphere by plotting $P(|s_3|)$ of all the points in the simulated speckle field. This is depicted in figure 3.4(d). We can only determine the absolute value, since we obtain s_3 from equation (2.11), which does not unambiguously determine the sign of s_3. It is however very clear that $P(|s_3|)$ is a uniform distribution. We have no reason to assume that $P(s_3)$ (so with positive and negative values distinguished) will not be uniform. That would mean there is a disproportionate fraction of vortices which is either positive or negative. This, however, we do not observe.

To conclude, the simulations indicate that the defined vortex properties indeed have statistics which were predicted by the theory in the previous chapter. Now, the most important question is if this is also observed in an experiment. That will be discussed in the next chapters.

Chapter 4

Data Analysis

The interference patterns generated by the MPI can be used to obtain the electric fields at the location of the pinholes of the MPI. This gives complete information about the speckle field and allows us to observe the properties of individual vortices.

To extract information on the fields from this pattern, it is necessary to understand how the interference pattern is formed. We will start with that discussion, before we solve the complex field amplitudes. Finally we will describe how we can obtain the circular first-order derivatives of the field, which we will need to describe the vortices.

4.1 Theory: interference pattern behind an MPI

A general MPI consists of N pinholes with diameter b. The pinholes are positioned on a circle with radius a. We assume that a and b are much smaller than the average speckle size such that (i) the field is constant over a single pinhole and (ii) only first derivatives of the field have to be included in the analysis.

The complex amplitudes directly at the pinholes are

$$E(x,y) = \sum_{m=1}^{N} E_m \mathrm{circ}(x - x_m, y - y_m), \tag{4.1}$$

where E_m represents the complex field amplitude at the m-th pinhole ($E_m = A_m e^{i\phi_m}$) and $\mathrm{circ}(x - x_m, y - y_m)$ is the transmission function of pinhole m, defined by

$$circ(x,y) = \begin{cases} 1 \text{ if } \sqrt{x^2+y^2} \leq b/2 \\ 0 \text{ if } \sqrt{x^2+y^2} > b/2. \end{cases} \tag{4.2}$$

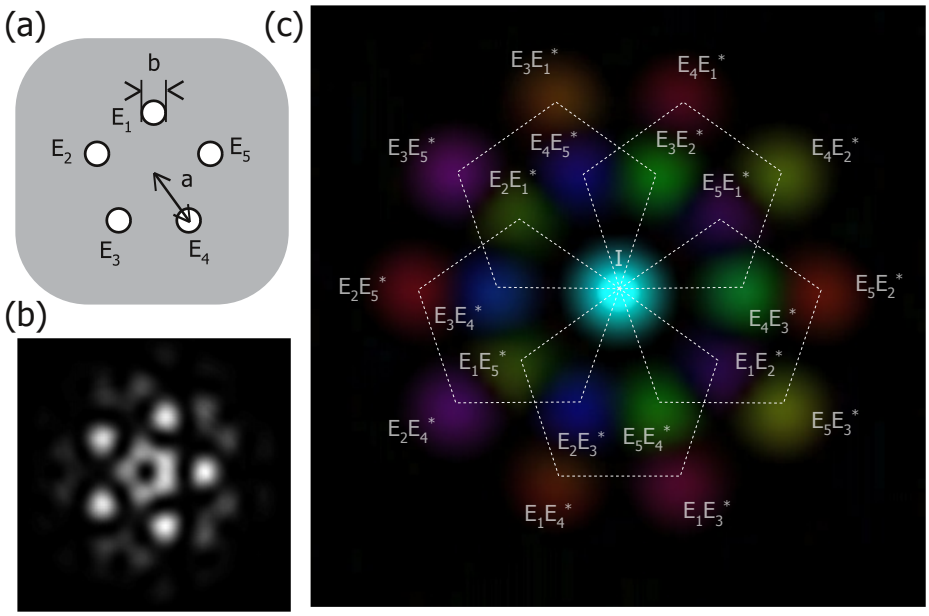

Figure 4.1: Illustration of the three steps in the analysis process. (a) The pinhole configuration for an MPI with N = 5. The fields impinging the pinholes are labeled E_m. (b) The far-field diffraction pattern of an optical vortex ($l = +1$) behind the MPI, as it is captured by a CCD-camera. (c) False colour plot of the Fourier transform of (b). The brightness of the colours represents the amplitude of the Fourier image, while the colours themselves depict the phase. The labels m, n of the fields $E_m^* E_n$ correspond to those in (a).

The coordinate (x_m, y_m) is the center of pinhole m, as given by

$$(x_m, y_m) = a\left(\cos\frac{2\pi m}{N}, \sin\frac{2\pi m}{N}\right). \tag{4.3}$$

The far field interference pattern of the light coming through the pinholes is given by

$$I(u,v) = I_0\Big|\sum_{m=1}^{N} E_m F\{\mathrm{circ}(x - x_m, y - y_m)\}\Big|^2, \tag{4.4}$$

where F denotes the Fourier transform.

This interference pattern can be analyzed quantitatively by taking the inverse Fourier transform of the interference pattern [8]:

$$g(x,y) = F^{-1}\{I(u,v)\} = I_0 \sum_{m,n=1}^{N} P_{mn}(x,y) E_m E_n^*, \tag{4.5}$$

where P_{mn} is the auto-correlation function of the pinholes:

$$P_{mn}(x,y) = \Big\langle \mathrm{circ}(x' - x_m, y' - y_m)\mathrm{circ}(x' - x_m + x, y' - y_m + y) \Big\rangle. \quad (4.6)$$

The Fourier transform $g(x,y)$ therefore comprises a series of $N(N-1)+1$ discrete spots, as depicted in figure 4.1(c). Each of these spots is the correlation of two pinholes m, n. The moduli of these spots are cone-shaped with peak values of $|g(x_m - x_n, y_m - y_n)| = I_0|E_m E_n^*|$. The single central spot is real-valued and has a peak value of

$$I = \sum_{n=1}^{N} |E_n|^2. \quad (4.7)$$

For a square CCD-image of n by n pixels of size d, the central position of the spots (x_{mn}, y_{mn}) in the expression of equation (4.5) in pixel units is

$$(x_{mn}, y_{mn}) = \frac{nd}{\lambda z}(x_m - x_n, y_m - y_n). \quad (4.8)$$

where z is the distance between the MPI and the CCD and λ is the wavelength of the light. The diameter of the spots in this inverse Fourier image of the interference pattern is

$$s = \frac{nd}{\lambda z} b. \quad (4.9)$$

4.2 Solving the complex field amplitudes

The analysis of the data starts with locating the spots in the Fourier image of the interference pattern. A good estimate can be made from eguation (4.8). The amplitudes (A_m) and phases (ϕ_m) have to be solved for separately.

Solving the amplitudes

We start by solving the amplitudes. These are obtained from the absolute value of the Fourier image $|g(x,y)|$. The peak values at each spot are obtained by fitting a cone to each of the spots:

$$f(x,y) = |S_{mn}| - b\sqrt{(x - x_{mn})^2 + (y - y_{mn})^2}. \quad (4.10)$$

The parameter of interest is the peak value $|S_{mn}|$, which is proportional to the product $|E_m E_n^*| = A_m A_n$.

Now we have to solve these products $A_m A_n$ for the amplitudes A_m. To obtain these solutions we look at the collection of spots where the index m remains fixed. This traces out polygons in the Fourier image. This is drawn for $N = 5$ in figure 4.1(c).

From the fitting routine we obtain the product of the amplitudes from the Fourier image

$$S_{mn} = A_m A_n. \tag{4.11}$$

The value of the center spot was given in 4.7 and can be rewritten in terms of S_{mn}:

$$I = \sum_{n=1}^{N} |E_n|^2 = A_m^2 + \sum_{n \neq m}^{N} \frac{S_{mn}^2}{A_m^2}. \tag{4.12}$$

Since I and S_{mn} are obtained from the Fourier image, we can solve for A_m^2:

$$A_m^2 = \frac{1}{2}\left(I - \sqrt{I - \sum_{n \neq m}^{N} S_{mn}} \right). \tag{4.13}$$

We can now use equation (4.11) to solve for the other amplitudes $A_{n \neq m}$. This analysis is repeated for the other $N-1$ polygons, reducing the errors in the determination of the amplitudes.

The background noise of the CCD-image accumulates in the central pixel of the Fourier transform, resulting in a systematically overestimated value for I. This is solved by omitting the central pixel from the fit routine.

Solving the phases

The phases on the pinholes are embedded in the Fourier image as phase differences $\phi_m - \phi_n$ at every spot. To obtain a more accurate value for this phase difference, the phase of each spot is obtained by averaging over four pixels in the center of the spot. When we again consider the polygons of fixed index m, we find for each m a series of N phase differences, which we can order in a vector:

$$\Delta\vec{\phi}_m = \begin{pmatrix} \phi_m - \phi_1 \\ \vdots \\ \phi_m - \phi_N \end{pmatrix}. \tag{4.14}$$

Since we can only know the phases at the pinhole relative to one another we set $\phi_1 = 0$. This gives us

$$\Delta\vec{\phi}_{m \neq 1} = \begin{pmatrix} \phi_m - 0 \\ \phi_m - \phi_2 \\ \vdots \\ \phi_m - \phi_N \end{pmatrix} \quad , \quad \Delta\vec{\phi}_1 = - \begin{pmatrix} 0 \\ \phi_2 \\ \vdots \\ \phi_N \end{pmatrix}. \tag{4.15}$$

In principle, we could read off the phases from the components of $\Delta\vec{\phi}_1$. However, if we want to achieve the same experimental accuracy in the determination of the phases as we attained in the determination of the amplitudes, we must average over the N times that the phase information is present in the Fourier image. We obtain this information by subtraction of the vectors

$$\Delta\vec{\phi}_{m\neq 1} - \Delta\vec{\phi}_1 = \begin{pmatrix} \phi_m \\ \vdots \\ \phi_m \end{pmatrix}. \tag{4.16}$$

Taking the average over all N components yields a value for ϕ_m.

In conclusion, this analysis yields values for the complex field amplitudes $E_m = A_m e^{i\phi_m}$ at all N pinholes, with phases relative to E_1.

Obtaining the derivatives of the field

Finally, we'd like to acquire an expression for the circular derivatives $\alpha_\pm$ of the field. To this end, reconsider equation 2.3. The α_+ and α_- are basically the weights of the $l = +1$ and $l = -1$ vortex modes. So we calculate the weight of each of the ring modes λ_l from the fields, by using the relation

$$\lambda_l = \sum_{n=1}^{N} E_n \, e^{-2\pi i n l/N}. \tag{4.17}$$

For an odd number N, there are N different ring modes that can be identified with the MPI [7], ranging from $l = -(N-1)/2$ to $+(N-1)/2$. So for $N = 5$, $l = 0, \pm 1, \pm 2$. These ring modes relate to the $\alpha_\pm$ from the previous chapter in the following way:

$$\begin{aligned} \lambda_0 &= \alpha_0 \\ \lambda_{\pm 1} &= a\,\alpha_{\pm 1} \end{aligned}, \tag{4.18}$$

where $a = \Delta r$ from equation (2.3). In a way the modal amplitudes λ_l are more natural than the field amplitudes α_0 and derivatives $\alpha_\pm$, since they all have the same units.

There is no direct relationship between λ_l's with $|l| \geq 2$ and higher order derivatives of the field. But higher order λ's can be interpreted as corrections to the linear expansion of the field around the center of the MPI.

Since we defined the phases of our fields with respect to a semi-arbitrary phase, namely that of E_1, the λ_l will also pick up an extra phase factor. This however does not matter, since we will only use their absolute values and relative phases. (see chapter 2)

Chapter 5

Experimental set-up

This chapter describes the experimental set-up. The set-up is shown in figure 5.1. Optical speckle is produced by illuminating a light shaping diffuser with a beam from a HeNe laser. At sufficient distance, where the speckle is fully developed, an MPI is mounted on a translation stage. A CCD-camera behind an f-f optical system records the far field diffraction pattern of the light passing through the MPI.

The MPI consists of 5 holes distributed uniformly on a circle with radius a. The size of the pinholes is denoted by b. The smallest available a (100 µm) is chosen to satisfy the linearization condition required for equation (2.1). The average speckle distance in our geometry is about $X_{sp} \sim 1$mm, so this should be small enough. Since we are most interested in the darkest areas in the speckle field, the largest available pinhole size b (50 µm) is chosen to maximize the throughput.

The translation stage can be moved in the x- and y-direction, so we can analyze the speckle field at different positions. We will scan the MPI through

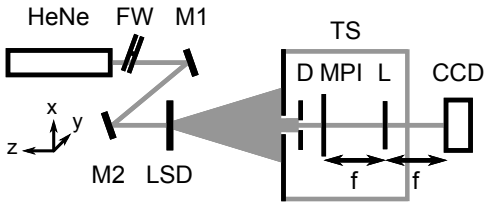

Figure 5.1: Schematic view of the setup used to detect optical vortices. After reflection of two mirrors (M1 and M2) a helium-neon (HeNe) laser beam illuminates a light shaping diffuser (LSD) to create a speckle pattern. Parts of the speckle pattern are allowed to pass through, onto a multi-pinhole interferometer (MPI). The resulting interference pattern is recorded by a CCD-camera (CCD). The MPI is mounted on a translation stage (TS) that can be moved in the x- and y-direction.

the speckle field in a square grid with distances of 10 to 40 µm. At every step an interference pattern is acquired and analyzed to obtain the complex fields at the pinholes and the corresponding ring mode decomposition, following the procedure described in the previous chapter.

Because the MPI moves through the speckle field while the CCD remains fixed, the central position of the interference pattern changes with every step of the translation stages. Therefore the image first has to be centered before the Fourier analysis is performed. Otherwise there will be a phase gradient in the Fourier image, rendering the analysis of the previous chapter useless. This centering is done by convoluting the image with a Bessel function. The maximum in the convolution corresponds to the center of the interference pattern. An image of 512×512 pixels is cut out around this center.

Chapter 6

Experimental results on a vortex beam

To support the validity of our method, we first present the experimental results of measurements on an isotropical vortex beam. Such a beam is produced by a so-called fork or edge dislocation hologram. Fork holograms, when illuminated with a laser beam, produce a far-field diffraction pattern with an optical vortex in each of the diffraction orders, except for the zeroth order (figure 6.1). The charge of the vortex corresponds to the number of the diffraction order. Since a speckle pattern contains almost exclusively $l = \pm 1$ vortices, we pick the diffraction order that contains a vortex with $l = 1$.

This vortex is scanned with the setup as described in chapter 5, where we replaced the light shaping diffusor by a fork hologram. We acquire 20×20 images of interference patterns with distances of 20 µm between each consecutive image. Each interference pattern is then analyzed with the method described in chapter 4, to yield the complex field amplitudes at each of the pinholes and the corresponding ring mode amplitudes λ_l.

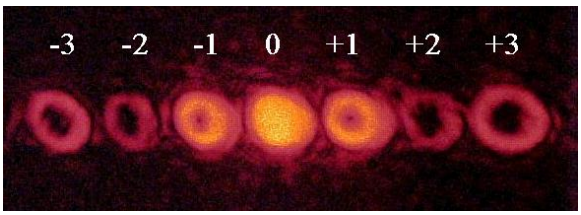

Figure 6.1: The diffraction pattern produced by a fork hologram. Each of the diffraction orders contains an optical vortex, with charge corresponding to the order of diffraction (except of course in the zeroth order). Photo by Azure Hansen, Stony Brook University, 2004. Released in the Public Domain.

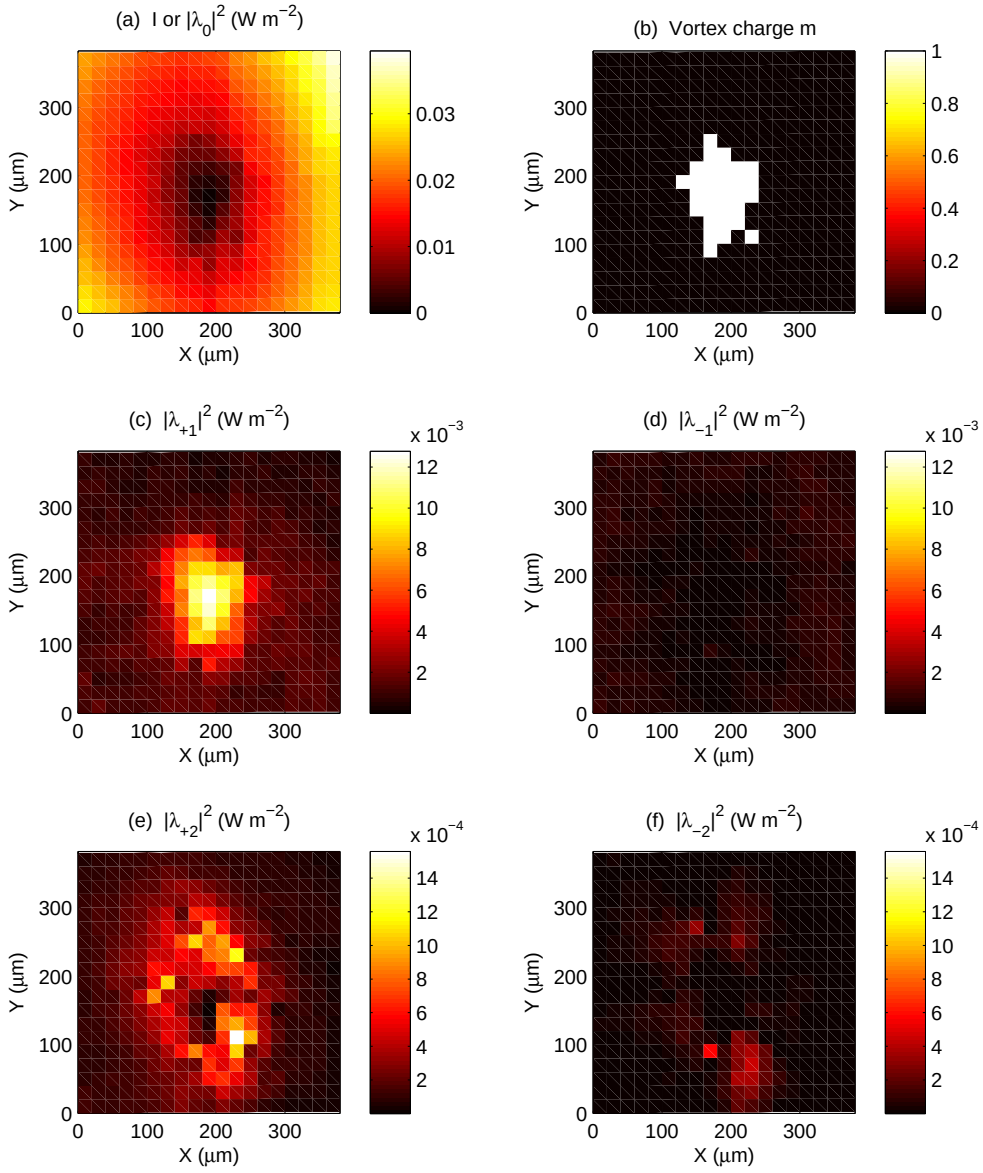

Figure 6.2: Detection of an optical vortex beam of $l = 1$. At intervals of 20 µm an image is acquired of the interference pattern behind the MPI. Each interference pattern yields a value for $|\lambda_l|^2$ (with l ranging from -1 to +1), which constitutes one pixel in the data shown here. (a) shows the intensity $|\lambda_0|^2$ of the vortex beam as function of position. (b) shows the vortex charge of the beam, determined by counting the phase discontinuities at each point. (c) and (d) show the intensities of the first-order modes $|\lambda_{+1}|^2$ and $|\lambda_{-1}|^2$, respectively; only the $l = +1$ mode gives a significant contribution. (e) and (f) show the intensities of the second order ring modes; these are significantly smaller.

The results of this series of measurements are shown in figure 6.2. 6.2(a) shows the intensity of the vortex beam. It shows that the scan was centered around a minimum of the intensity. In figure (b) the net vortex charge is plotted at every measured position. This was determined by use of the phase unwrapping method, described in chapter 3. The shape of a pentagon is clearly visible in this image. This corresponds to the pentagon-shaped MPI we used and means that an isotropic vortex will only be detected when it is inside the configuration of pinholes.

Figures 6.2(c)-(f) show the intensities $|\lambda_l|^2$ higher-order ring modes. As expected, only the λ_{+1} mode gives a significant contribution in the center of the beam. In fact, roughly at the positions of the detected vortex it dominates over the λ_0 contribution.

The intensities $|\lambda_{\pm 2}|^2$ of the higher order modes are about an order of magnitude weaker than the $|\lambda_1|^2$. The $l = +2$ component, with the same sign as the vortex charge, is the one that gives the largest contribution of the two. This concurs with the observation that a vortex that is aligned off-center in the MPI will mix in $l = \pm 2$ components into the interference pattern [11].

With the equations (2.10) that relate ϵ, ϕ_0 to $\alpha_\pm$ and (4.18) that relates $\alpha_\pm$ to $\lambda_{\pm 1}$, we can calculate the elliptic properties of this vortex:

$$\begin{aligned} \epsilon &= 0.19 \\ \phi_0 &= \text{-}0.48\pi \end{aligned}$$

We can relate this to the description in terms of Stokes vectors with equation (2.11), which yields

$$s_3 = 1.00$$

We observe that the experiment on a vortex beam yields the desired results. This supports the theory laid out in the first chapters. We will perform the same experiments on speckle patterns in the next chapter.

Chapter 7

Experiments on optical speckle

In this chapter we present the results of experiments on optical speckle patterns. We will treat the properties of the vortices in the speckle pattern in a statistical fashion, leaning heavily on the theory of chapter 2 and compare the results to the simulations from chapter 3.

7.1 Experimental results

We present the results of three independent experiments. They differ in the step size between successive image acquisitions and in the total scanned area.

Dataset	Step size	Scanned area
A	10 µm	800×800 µm^2
B	20 µm	4000×4000 µm^2
C	40 µm	6400×6400 µm^2

Figure 7.1 shows the result of measurement A, which was done on a single vortex in a speckle pattern. Steps of 10 µm were made between each acquisition of an interference pattern. Figure 7.1 shows the same trends as figure 6.2, albeit less smooth, as expected from a speckle pattern. The vortex charge as determined by the phase unwrapping method in (b) shows a single vortex of charge $m = +1$, in the darkest part of the speckle pattern. Correspondingly in (c) the $|\lambda_{+1}|^2$ mode lights up at the same position. In (d) the contribution of $|\lambda_{-1}|^2$ is visible, but it is negligible at the vortex. The contribution from the higher order ring modes $|\lambda_{\pm 2}|^2$ is again an order of magnitude smaller. The mode with the same sign as the vortex, in this case $|\lambda_{+2}|^2$, still dominates over the mode with opposite sign.

It is remarkable to see that the elevated values of $|\lambda_{+1}|^2$ extend to beyond the positions where the vortex falls within the MPI. There also seems to be

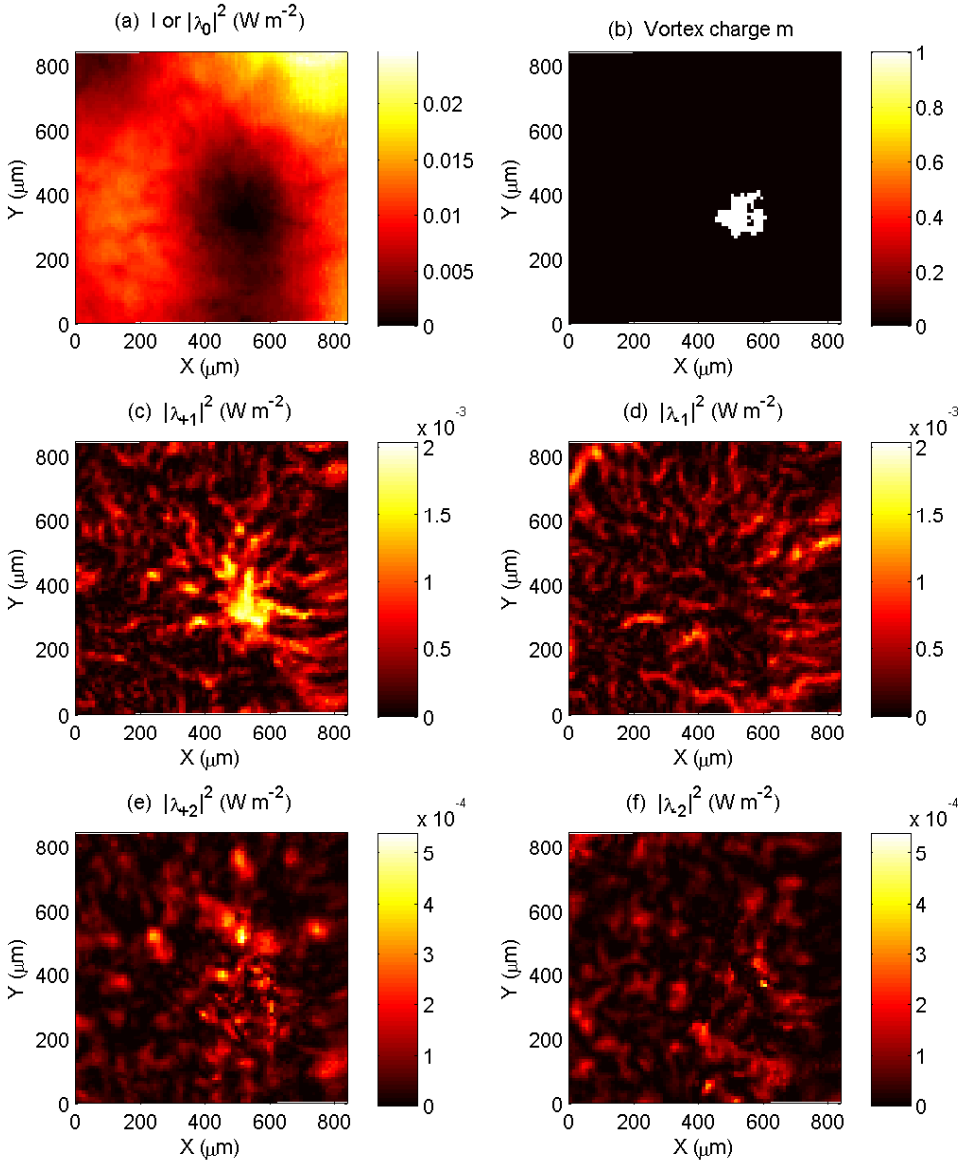

Figure 7.1: The results of measurement A on a single optical vortex ($m = +1$) in a speckle pattern. Steps of 10 μm were made. (a) shows the intensity of the speckle pattern. The position and charge of the vortex is determined in (b) by looking at phase jumps at the pinholes which are larger than π. (c)-(f) depict the modal intensities $|\lambda_l|^2$. It is obvious that the only significant contribution at the vortex position is from the $|\lambda_{+1}|^2$ component. The $|\lambda_{\pm 2}|^2$ components are again much smaller than the $|\lambda_{\pm 1}|^2$.

a substructure in the speckle of this mode, which was not observed in the experiment on the vortex beam.

The properties of this vortex are calculated:

$$\begin{aligned} \epsilon &= 0.88 \\ \phi_0 &= \text{-}0.05\pi \\ s_3 &= 0.77 \end{aligned}$$

Figure 7.2 shows a plot of measurement B. Steps of 20 µm were taken between consecutive probings of the field. There are several vortices visible in (b). The vortices shown in (b) can visually be correlated with the bright spots in the plots of $|\lambda_{\pm 1}|^2$ in (c) and (d). There are a few pairs of oppositely charged vortices close together, where it is hard to separate them. The attraction and repulsion of vortices has been studied in more detail in [12].

The second-order ring modes are again small, save a few bright points which we can further neglect. The second-order modal amplitudes do however respond to the presence of vortices. Bright spots in $|\lambda_{\pm 2}|^2$ are visible in the same areas as the first-order ring mode with concurrent sign.

Measurement C is a scan over an area of 6.4×6.4 mm speckle field, with step sizes of 40 µm. Figure 7.3 shows plots of a 3.6×3.6 mm section of that measurement. With the stepsize of 40 µm we are still able to locate the vortices with the criterium of phase discontinuities (b). Again we see pairs of oppositely charged vortices close together. However it is now hard to visually correlate these vortices to bright spots in the plots of (c) λ_{+1} and (d) λ_{-1}.

So a more quantitative method is required to obtain the vortices from the speckle pattern using the ring modes λ_l. We propose a method where the largest of the modes $|\lambda_0|^2$, $|\lambda_{+1}|^2$ and $|\lambda_{-1}|^2$ determines the vortex charge to be 0, +1 or -1, respectively. The results hereof applied on measurement C are shown in figure 7.4(b), alongside the results of the phase unwrapping method in (a). The intensity is plotted, with the vortices highlighted in white. First of all, note that the vortices only occur in dark spots of the speckle pattern. More importantly, both methods seem to be able to detect optical vortices in a speckle pattern. As mentioned before, the method of (b) seems to detect the vortices in a larger area than just the area of the MPI.

In order to perform a statistical analysis on just the vortices, it is important which of these methods is more accurate. If either too many or too few points in the field are marked as vortex, the statistics will be biased either towards the statistics of the whole speckle field or towards the statistics of a subset of the vortices.

Method (b) seems to be better equipped to deal with more elongated vortex structures, where the ellipticity ϵ is probably very high. We see this in figure 7.4(b), where the amount of detected vortex points increases drastically in the dark 'gutters' of the speckle field. In the extreme case of

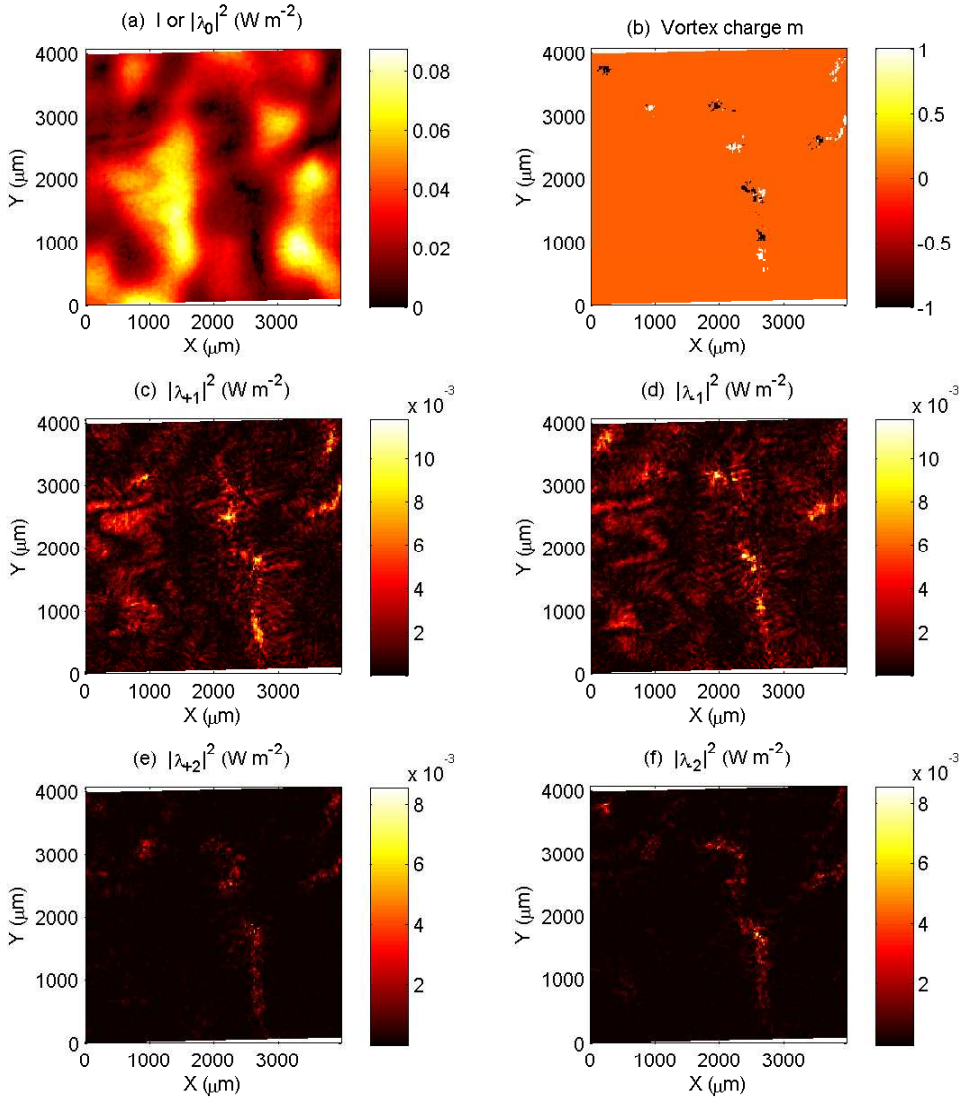

Figure 7.2: The results of measurement B on an optical speckle pattern. The step size is 20 μm. (a) shows the intensity of the speckle pattern. The positions of the vortices are determined in (b) by looking at phase jumps. The positions and charges of these vortices clearly match the positions in (c) and (d) where $|\lambda_{+1}|^2$ and $|\lambda_{-1}|^2$ light up.

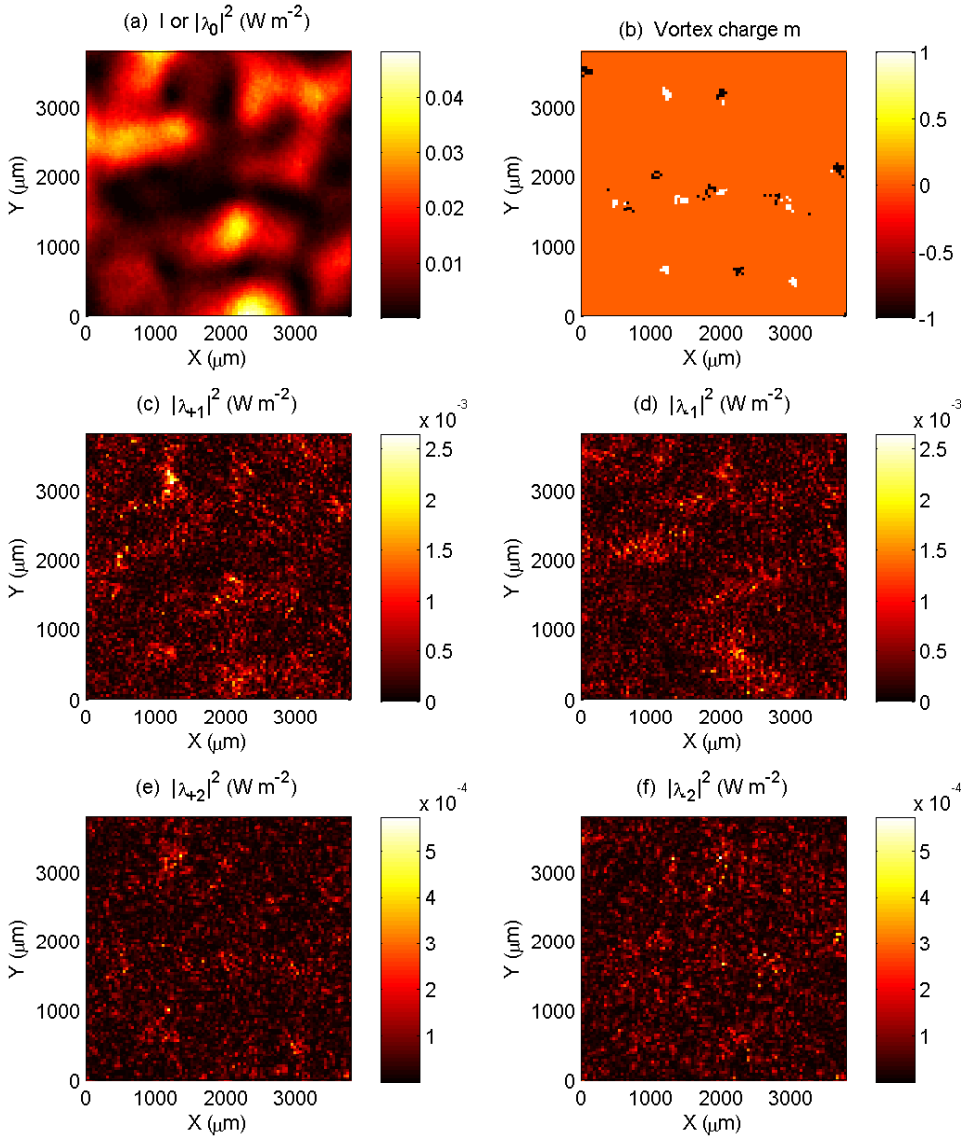

Figure 7.3: The results of measurement C on an optical speckle pattern with a step size of 40 µm. For visibility only a quarter of the scanned area of 6400×6400 µm^2 is shown. (a) shows the intensity of the speckle pattern. The positions of the vortices can still be determined in (b), but it is however more difficult to correlate these vortices to light spots in the plots of $|\lambda_{\pm 1}|^2$ in (c) and (d).

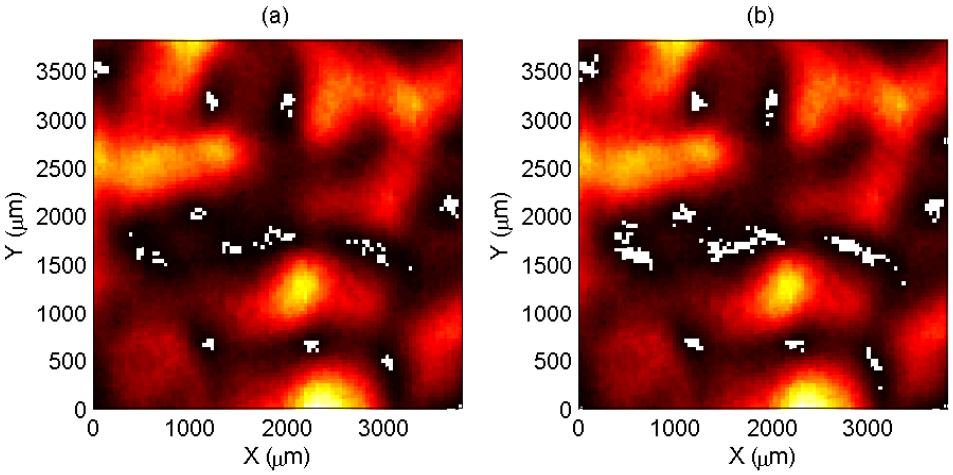

Figure 7.4: The intensity of experiment C with +1 and -1 vortices highlighted in white. In (a) the vortices are detected by the presence of phase unwrapping, while in (b) the largest of the modes $|\lambda_0|^2$, $|\lambda_{+1}|^2$ and $|\lambda_{-1}|^2$ determines the vortex charge. The obtainedd results are comparable, but both methods yield an unexpected and seamingly noisy structure.

$\epsilon = 1$ (or $s_3 = 0$) the vortex is linear. Then there are two phase jumps on a contour around the vortex. This means that the phase unwrapping method will give a vortex charge of zero, hence the vortex is not detected.

On the other hand, since the vortex is a point structure, it seems more natural to pick the method which confines the location of the vortices the most. This would favour method (a). Method (b) indicates a bigger spread in the position of the vortices. A good fraction of the points marked as optical vortex does not actually contain a vortex and will not obey the statistics expected for the vortices.

We will continue to work with method (a), since it yields less false positive reports of a vortex.

The auto-correlation functions of the field and the first-order ring modes is determined from measurement C. The results are plotted in figure 7.5. Because of the limited number of data points in a measurement, the statistics are not sufficient for a quantitative comparison with the simulations. We can, however, point out similar trends. First of all, the autocorrelation of the field show a reasonably Gaussian profile. The correlation function of the ring modes $l = \pm 1$ definitely has a smaller width than the $l = 0$ mode, but does not show a Gaussian profile (being more strangely peaked in the center), nor any clear dips to the side of the central peak. Only a significantly larger set of data points would allow for a more accurate plot and a quantitative comparison.

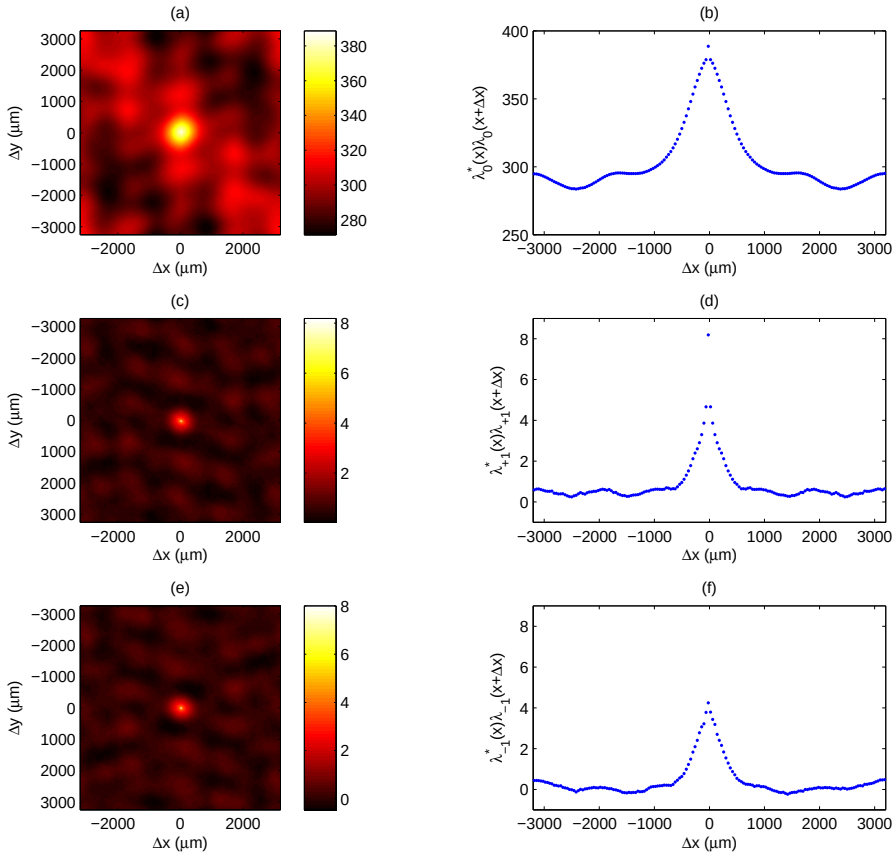

Figure 7.5: Auto-correlation functions corresponding to measurement C. Auto-corelation of (a) the speckle field E, (c) α_+ and (e) α_-. The graphs (b), (d) and (f) show intersections along the x-axis of the left figures.

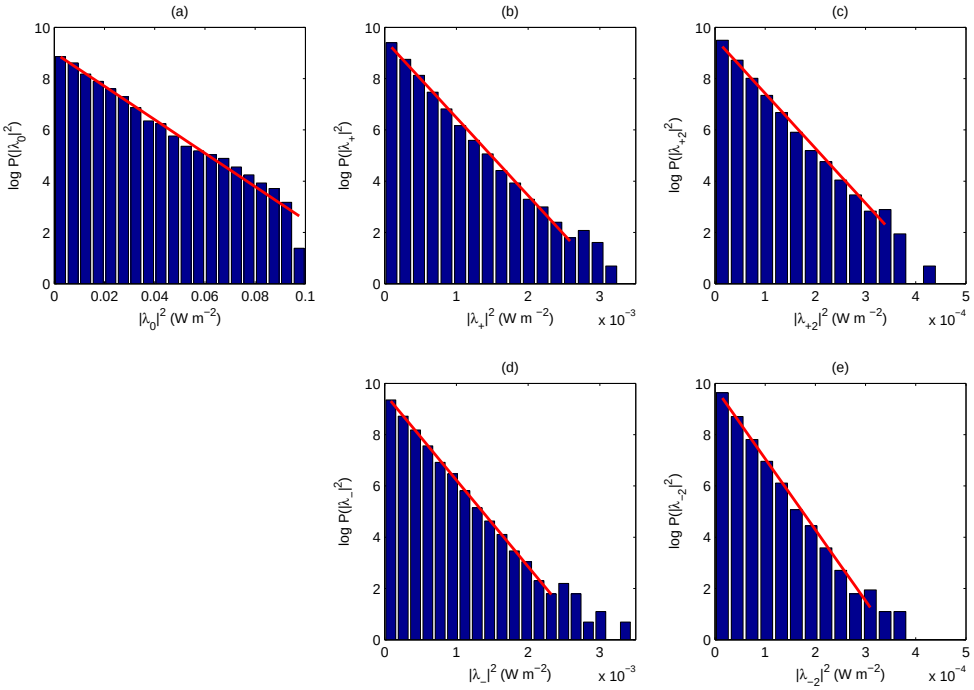

Figure 7.6: From a collection of five experiments the statistical distributions of the different l-modes is calculated. As expected, in (a), $|\lambda_0|^2$ or I is distributed exponentially, with average value $W_0 = 0.0153$ W m^{-2}. In (b) $|\lambda_{+1}|^2$ and (c) $|\lambda_{-1}|^2$ yield a similar exponential distribution, also as expected, with average values of $W_{\lambda_{+1}} = 3.29 \times 10^{-4}$ W m^{-2} and $W_{\lambda_{-1}} = 2.97 \times 10^{-4}$ W m^{-2}. Finally, the second order modes in (d) and (e) are also exponentially distributed with average values of $W_{\lambda_{+2}} = 4.67 \times 10^{-5}$ W m^{-2} and $W_{\lambda_{-2}} = 3.61 \times 10^{-5}$ W m^{-2}.

7.2 Statistics

To perform a statistical analysis on the speckle, we used five different datasets, including measurements B and C. These consist in total of more than 150,000 data points, of which over 2,000 points are indicated as vortices. This number makes a statistical analysis meaningful and allows us to compare such an analysis with the simulations from chapter 3.

The probability distributions of the different λ_l are plotted in figure 7.6. As expected, the intensties $|\lambda_0|^2$ and $|\lambda_{\pm 1}|^2$, and even $|\lambda_{\pm 2}|^2$ are distributed exponentially. Similar to the simulations, we fit the logarithms of these distributions to obtain average values W_{λ_l} over the speckle field:

$$P(|\lambda_l|^2) = P_0 e^{-|\lambda_l|^2/W_{\lambda_l}}. \tag{7.1}$$

The zeroth and first order modes can be quantitatively compared with

the probability distributions of the $\alpha_{0,\pm}$ modes in figure 3.1, since they differ by a constant factor a (see eq. 4.18). For these modes we calculate the ratios:

$$\begin{aligned} \frac{W_0}{W_{\lambda_{+1}}} &= 46.5 \\ \frac{W_0}{W_{\lambda_{-1}}} &= 51.6 \end{aligned} .$$

The ratios

$$\begin{aligned} \frac{W_{\lambda_{+1}}}{W_{\lambda_{+2}}} &= 7.05 \\ \frac{W_{\lambda_{+1}}}{W_{\lambda_{-2}}} &= 8.22 \end{aligned}$$

indicate if the linearization of the field is a valid approximation. These ratios are larger than unity, although not much larger. This means we are at the limits of the linearization condition.

To verify that λ_{+1} and λ_{-1} are indeed independent, as the simulations predict, we apply the same method as we did for the simulated speckle. Formula 3.3 can be restated in terms of λ_l

$$F = \int \sqrt{P\big(|\lambda_{+1}|^2, |\lambda_{-1}|^2\big)}\, \sqrt{P\big(|\lambda_{+1}|^2\big) P\big(|\lambda_{-1}|^2\big)}\, d|\lambda_{+1}|^2 d|\lambda_{-1}|^2, \quad (7.2)$$

assuming the involved probability distributions are normalized. A calculation yields a value of $F = 0.992$. It can thus be safely concluded that λ_{+1} and λ_{-1} are indeed statistically independent.

The most important aspect to uncover is the statistical behaviour of the vortex properties in terms of its elliptic properties ϵ and ϕ_0 and in terms of the stokes parameter s_3. The resulting histograms are plotted in figure 7.7(a)-(c).

The result is exactly the same as what we obtained with simulations of a specklefield (figure 3.4). The experimental distribution of ϵ is plotted alongside the theoretical prediction. It reproduces the distribution that was found by [6]. The orientation ϕ_0 is uniformly distributed between $-\pi$ an π, indicating isotropy in the speckle field.

The distribution of s_3^2 at the vortices from the simulations is perfectly reproduced, including the sharp peak towards $s_3^2 = 0$. Besides that the distribution is uniform, validating the description in terms of Stokes vectors as a natural one.

Figure 7.7(d) again shows the distribution of $|s_3|$ over the entire specklefield. The fact that this distribution is uniform means that the derivatives of a speckle field can be represented as a uniform quantity over the Poincaré sphere.

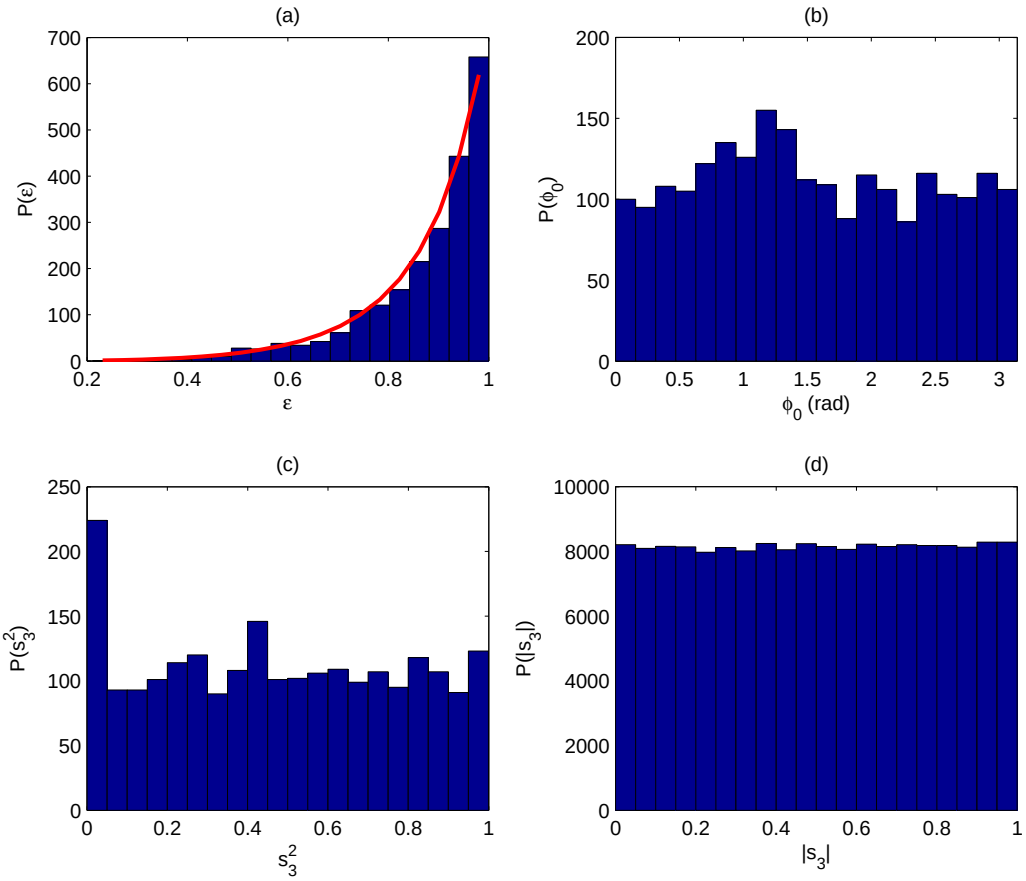

Figure 7.7: Figures (a), (b) and (c) depict the measured probability distributions of the different vortex parameters; ϵ, ϕ_0 and s_3^2. Figure (d) depicts the distribution of $|s_3|$ over the entire specklefield.

Chapter 8

Conclusion and discussion

8.1 Conclusion

In chapter 2 we saw that a speckle field could locally be expanded in first-order derivatives of the field. We defined circular derivatives α_+ and α_-, which were the amplitudes in a linear combination of an $m = +1$ and an $m = -1$ vortex, respectively. In chapter 4 we described how a Multi-Pinhole Interferometer (MPI) could be used to find these circular derivatives experimentally. An MPI is a small structure and therefore suitable for probing the local optical field. The field on the pinholes can be determined up to a single phase. Chapter 6 described the proof of concept with measurements of a vortex beam. In chapter 7 the results of measurements on a speckle pattern were presented. We were able to fully reconstruct the local field and the circular derivatives of the speckle field in a 2D plane.

In the theory we argued for a description of a vortex with two independent properties, namely the eccentricity ϵ of the phase gradient and the orientation ϕ_0 of the resulting ellipse (chapter 2). These properties can be calculated from the derivatives of the electric field. We could therefore also determine these properties experimentally. In chapter 6 this was done for a single optical vortex in a vortex beam. In chapter 7 the properties ϵ and ϕ_0 were measured on many vortices, allowing for a statistical analysis. This matched predictions made by theory (chapter 2) and simulations (chapter 3).

We showed that the speckle field could also be characterized with Stokes vectors on the Poincaré sphere. We stated that the speckle field would be distributed uniformly over the Poincaré sphere. In chapter 2 we made the specific prediction that there is a uniform distribution along the s_3 direction. The vortices constitute special points in the speckle field and obey different statistics. We predicted that the vortices ar distributed uniformly in s_3^2, rather than in s_3. Both these predictions were confirmed by simulations (chapter 3) and experiments (chapter 7).

It is however still unclear why the probability distribution $P(s_3^2)$ of the vortices has a sharp peak at $s_3^2 = 0$, both in the experiment and the simulations. The situation where $s_3^2 = 0$ represents very elliptic - or even linear - vortices, so a study of this type of vortices could elucidate this observation.

8.2 Discussion: possible future experiments

Now that we have fully developed a method to probe speckle patterns, many more experiments can be designed to study speckle. First of all we note that an increase of the number of pinholes (N) will benefit the accuracy in the determination of the electric fields. In this thesis the principle of the MPI was demonstrated with $N = 5$, the minimum number at which the fields can be determined in ring modes up to order $l = \pm 2$. However, when $N = 7$ or higher are used (pinholes with even numbers of N don't distinguish between l and $-l$) the accuracy in the determination of the ring modes increases, since there are more data points in the sum in equation (4.17). This is especially true for anisotropic vortices, where the phase may change rapidly between adjacent pinholes.

A possible employment for the MPI would be as a wavefront-sensor, in the sense of a Shack-Hartmann detector. A Shack-Hartmann sensor can detect the local tilt of a wavefront, but does not respond to singularities in the phase. An MPI can detect singularities as well as tilts in the wavefront, so it can potentially improve the workings of such a device. Since a vortex is a point object and has no internal structure, it could fall between adjacent MPI's. However, when vortices are detected by looking at the first-order derivatives, we've seen that vortices can also be detected when the vortex does not fall into the MPI (see figure 7.4). Alternatively, the array could be translated laterally to create a resolution smaller than the radius of the MPI. If steps of $0.2a$ are taken, only 25 steps would have to be made to obtain the same resolution obtained in this thesis.

For further studies of the behaviour of vortices in a speckle pattern, the field can also be scanned in the z-direction, the direction of propagation. In our experiments this distance was fixed, but other experiments have been done where the speckle field was studied at different positions of z [14]. A possible subject of study could then be the attraction or repulsion of vortices with opposite or equal charges. This topic is to some extent already studied theoretically in ref. [12]. It could for instance be expected that this attraction and repulsion will be visible in the correlation function $\langle\, \lambda_+^*(\vec{x})\, \lambda_-(\vec{x} + \Delta\vec{x})\, \rangle$.

An attempt can even be made to let two equally charged vortices fuse to make an $l = \pm 2$ vortex. This last experiment could also be done by lateral translation of the diffusor plate in our experiment. The resulting change in the speckle pattern will reflect the rough and discrete structure of the

diffusor plate. It is unclear if the corresponding displacement of vortices is predictable. This is required to be able to control their movements.

The advantage of the MPI is that it can be scaled to arbitrary size, since only a finite number of point detectors is needed. In this light, an interesting observation we made was the fact that detection of vortices could also be possible with two pinholes. This could be interesting for applications where it is either too costly or inconvenient to work with multiple 'pinholes'. Here one of the pinholes overlaps with a vortex, where the phase changes arbitrarily fast, while the other serves as a source of a plane wave. A condition for this to work is that there is no vortex impinging the second pinhole. When an inverse Fourier transform is made of the resulting interference pattern (corresponding to $g(x, y)$ from equation 4.5 and figure 4.1(c)), the $E_1^* E_2$ and $E_2^* E_1$ spots show a fork-like phase profile, which allows for the determination the vortex charge. Once you determine on which of the pinholes the vortex impinges, the position of the vortex can even be determined up to the size of the pinholes, b.

Bibliography

[1] I. Freund and A. Belenkiy, "Higher-order extrema in two-dimensional wave fields," J. Opt. Soc. Am. A **17**, 434–446 (2000).

[2] I. Freund, "Optical vortices in gaussian random wave fields: statistical probability densities," J Opt Soc Am A **11**, 1644–1652 (1994).

[3] Y. Y. Schechner and J. Shamir, "Parameterization and orbital angular momentum of anisotropic dislocations," J Opt Soc Am A **13**, 967–973 (1996).

[4] M. R. Dennis, "Local phase structure of wave dislocation lines: twist and twirl," J Opt A-Pure Appl Op **6**, S202–S208 (2004).

[5] N. B. Baranova, B. Y. Zel'dovich, A. V. Mamaev, N. F. Pilipetskii, and V. V. Shkukov, "Dislocations of the wavefront of a speckle-inhomogoneous field (theory and experiment)," Jetp Lett+ **33**, 195–199 (1981).

[6] W. Wang, N. Ishii, S. G. Hanson, Y. Miyamoto, and M. Takeda, "Phase singularities in analytic signal of white-light speckle pattern with application to micro-displacement measurement," Opt Commun **248**, 59–68 (2005).

[7] G. C. G. Berkhout and M. W. Beijersbergen, "Method for probing the orbital angular momentum of optical vortices in electromagnetic waves from astronomical objects," Phys Rev Lett **101**, 100801 (2008).

[8] C.-S. Guo, S.-J. Yue, and G.-X. Wei, "Measuring the orbital angular momentum of optical vortices using a multipinhole plate," Appl. Phys. Lett. **94**, 231104 (2009).

[9] M. R. Dennis, "Topological singularities in wave fields," thesis pp. 1–246 (2001).

[10] J. W. Goodman, *Speckle phenomena in optics* (Roberts & Company, 2006).

[11] G. C. G. Berkhout and M. W. Beijersbergen, "Using a multipoint interferometer to measure the orbital angular momentum of light in astrophysics," J Opt A-Pure Appl Op **11**, 094021 (2009).

[12] I. Freund, N. Shvartsman, and V. Freilikher, "Optical dislocation networks in highly random media," Opt Commun **101**, 247–264 (1993).

[13] G. C. G. Berkhout, M. P. J. Lavery, J. Courtial, M. W. Beijersbergen, and M. J. Padgett, "Efficient sorting of orbital angular momentum states of light," Phys Rev Lett **105**, 153601 (2010).

[14] K. O'Holleran, M. Dennis, F. Flossmann, and M. Padgett, "Fractality of light's darkness," Phys. Rev. Lett. **100**, 053902 (2008).